Backscattering Differential Ghost Imaging in Turbid Media

M. Bina,[1,*] D. Magatti,[1,†] M. Molteni,[1] A. Gatti,[2,1] L. A. Lugiato,[1] and F. Ferri[1]

[1]*Dipartimento di Scienza e Alta Tecnologia, Università degli Studi dell'Insubria, Via Valleggio 11, I-22100 Como, Italy*

[2]*Istituto di Fotonica e Nanotecnologie-CNR, Piazza Leonardo da Vinci 32, I-20133 Milano, Italy*

(Received 9 August 2012; published 19 February 2013)

In this Letter we present experimental results concerning the retrieval of images of absorbing objects immersed in turbid media via differential ghost imaging (DGI) in a backscattering configuration. The method has been applied, for the first time to our knowledge, to the imaging of thin black objects located inside a turbid solution in proximity of its surface. We show that it recovers images with a contrast better than standard noncorrelated *direct* imaging, but equivalent to noncorrelated *diffusive* imaging. A simple theoretical model capable of describing the basic optics of DGI in turbid media is proposed.

DOI: 10.1103/PhysRevLett.110.083901 PACS numbers: 42.30.−d, 42.50.Ar, 87.85.Pq

Ghost imaging (GI) is an optical technique for the retrieval of images via intensity correlation of two light beams. The first experimental approach and theoretical explanation of GI was quantumlike [1], but after a long-standing debate [2], it was finally demonstrated that GI can be also realized with classical light beams [3,4]. Thermal GI, for instance, is performed with two spatially correlated speckle beams obtained by means of a rotating ground glass and a beam splitter. The object beam illuminates the object and is collected by a bucket detector with no spatial resolution, while the reference beam is recorded by a spatial-resolving detector, e.g., a charge coupled device (CCD) camera. Recent improvements of the GI protocol include computational GI, which uses computer controlled spatial light modulators [5], compressive sensing GI where the algorithm for the data analysis benefits from the sparsity properties of the object [6], and differential ghost imaging (DGI), which has been shown to perform much better than conventional GI when imaging weakly absorbing objects [7].

The potentialities of GI with respect to noncorrelated imaging stems from its ability to form images without the need of any pixelated detector placed near the object. Thus, GI is a good candidate for imaging objects immersed in optically harsh or noisy environments such as in a turbid medium or in the presence of optical aberrations. Recent applications in this direction include GI in the presence of atmospheric turbulence [8], fluorescent GI [9], and transmission GI in scattering media [10]. All these works have raised the interesting debate about whether GI is intrinsically more powerful than noncorrelated imaging and can be used, for example, as a remote sensing technique *immune* from atmospheric turbulence [11].

We propose in this Letter, for the first time to our knowledge, the use of DGI for retrieving the transmittance of absorbing objects immersed in a turbid medium, in proximity of its surface. We adopt a backscattering configuration of the bucket light detection, which is of interest e.g., for biomedical tissue imaging, where illumination and detection is performed on the same side. We compare DGI with two noncorrelated imaging techniques. Our results show that DGI performs much better than standard imaging, which uses direct illumination of the object. However when compared with nonstandard imaging, which uses a diffusive illumination, the two techniques are fairly equivalent.

The experimental setup for the DGI configuration is sketched in Fig. 1. The pseudothermal source, operating at $\lambda = 0.532$ μm, produces a rectangular collimated beam of *deep Fresnel* speckles [12] with a constant transversal size $\delta_x \simeq 82$ μm and longitudinal coherence length $\delta_z \sim \pi\delta_x^2/\lambda \simeq 40$ mm [13]. The beam area is $A_b = 44$ mm^2 and contains $N_{\text{speckle}} \simeq 6500$ speckles. The reference beam intensity $I_2(\mathbf{x}_2)$ is recorded at a distance $z_2 \simeq 250$ mm from the source by a CCD camera with pixel size 6.67 μm $\ll \delta_x$. The intensity $I_1(\mathbf{x}_1)$ hits the object at a distance $z_1 = z_2$ and is collected with a bucket detection in backscattering. The object, characterized by a spatial transmittance $T(\mathbf{x})$ over the same area of the beam, is immersed in a turbid solution contained in a cylindrical cell (diameter = 44 mm, length = 60 mm) and it is allowed to move along the optical axis. The turbid solution is made of an aqueous solution of polydisperse silica particles

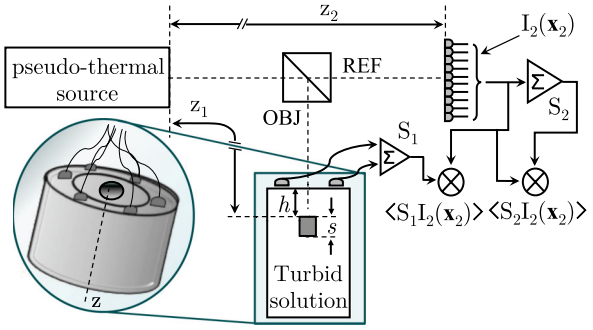

FIG. 1 (color online). Setup for backscattering DGI. The zoom shows a detail of the scattering cell with the six photodiodes used for the bucket detection.

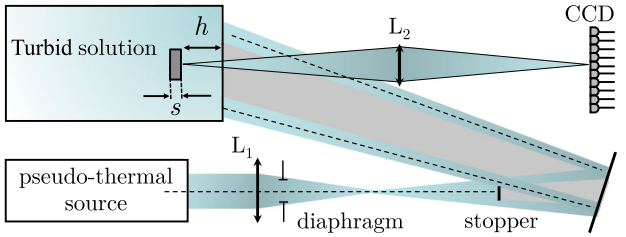

FIG. 2 (color online). Setup for direct and diffusive imaging. The object area is illuminated with a speckled light beam reshaped by lens L_1 and a diaphragm. The ring illumination for diffusive imaging is obtained placing a stopper. The lens L_2 realizes a 1:1 imaging of the object on the CCD sensor.

(Ludox PW-50, average particle diameter $\simeq 50$ nm). Three volume fractions, $\phi_1 = 3.1 \times 10^{-3}$, $\phi_2 = 7.8 \times 10^{-3}$, and $\phi_3 = 15.6 \times 10^{-3}$ were used, with corresponding transport mean free paths $l_1^* \simeq 17.3$ mm, $l_2^* \simeq 6.7$ mm, and $l_3^* \simeq 3.8$ mm. The light transmitted by the object and diffused by the medium is collected in backscattering by six photodiodes placed in a ring configuration (the ring radius is 15 mm) outside the cell around the illuminating beam. Such a configuration ensures that the average output signal from the six photodiodes can be used as an effective bucket detector. Indeed, the l^*'s of our media are much smaller than the average contour length L_c that photons travel from the injection point to the escaping point at the photodiodes positions. Thus, thanks to the backscattering detection, the light reaching the photodiodes is completely randomized and the measured signal is proportional to the overall power injected into the solution and transmitted by the object. This implies that, in a blank measurement with no object, $S_1^{\mathrm{blk}} = \alpha S_2$, where $S_2 = \int_{A_b} I_2(\mathbf{x_2}) d\mathbf{x_2}$ and α is a factor which takes into account any unbalancing (beam splitter, detectors, random medium) between the two arms.

The GI analysis is carried out by using the DGI algorithm [7] based on the measurement of the observable

$$\langle O_-(\mathbf{x_2})\rangle = \langle S_1 I_2(\mathbf{x_2})\rangle - \frac{\langle S_1\rangle}{\langle S_2\rangle}\langle S_2 I_2(\mathbf{x_2})\rangle, \qquad (1)$$

where S_1 and S_2 are the bucket signals collected in the object and reference arms, respectively, and $\langle\cdots\rangle$ is performed over different speckles configurations. From Eq. (1) we recover the fluctuations $\delta T_m(\mathbf{x})$ of the object transmittance, while the spatially averaged transmission function is retrieved from $\overline{T}_m = \langle S_1\rangle/(\alpha\langle S_2\rangle)$. The measured transmittance of the object is thus computed as $T_m(\mathbf{x}) = \overline{T}_m + \delta T_m(\mathbf{x})$.

The recovered ghost images are compared with *diffusive* and *direct* imaging performed with the setup shown in Fig. 2. Diffusive imaging is realized by illuminating the cell with a ring of speckled light, formed by reshaping the speckle beam with a diaphragm and a stopper. In this way the light diffused by the turbid medium, with $l^* \ll L_c$, uniformly transilluminates the object from the "rear." To our knowledge, this is the first time that such a setup has been proposed for the imaging of absorbing objects close to the medium surface. A similar approach was used very recently for oblique back-illumination microscopy [14]. In both cases the light diffused by the turbid medium realizes an effective transillumination of an object close to the surface of the medium. Direct imaging is, conversely, a standard epi-illumination method realized shining light directly on the object (the same setup of Fig. 2 with no stopper), as is customarily done in dermoscopy [15]. Both in diffusive and direct imaging, a macro objective (Nikon AF Micro Nikkor 60 mm $f/2.8$D) realizes a 1:1 imaging of the object onto the CCD sensor.

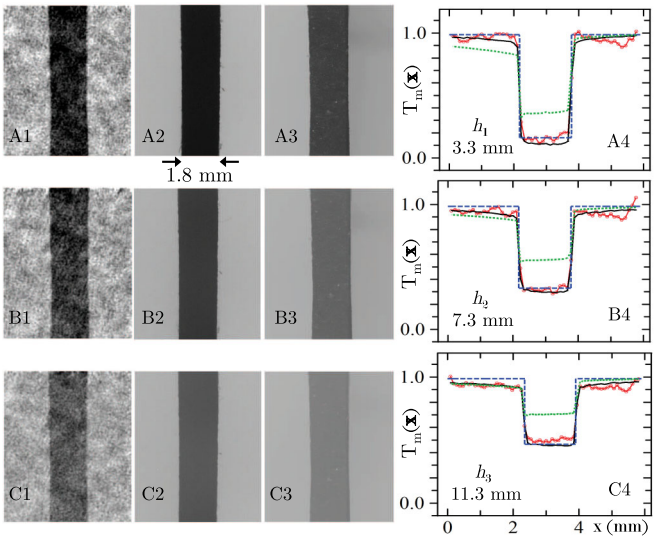

FIG. 3 (color online). Images of a thin black cardboard (section 1.8 mm × 8 mm, thickness $s \simeq 400$ μm) inside a turbid solution with $l^* = 17.3$ mm at $h_1 = 3.3$ mm (row A), $h_2 = 7.3$ mm (row B), and $h_3 = 11.3$ mm (row C), obtained with DGI (column 1), diffusive imaging (column 2), and direct imaging (column 3). Column 4 plots the corresponding horizontal sections averaged over the vertical size of the image: DGI (red wavy curve), diffusive imaging (black smooth curve), direct imaging (green dotted curve), and theoretical model (blue dashed line).

We considered two simple objects characterized by a binary transmission function, with $T(\mathbf{x}) = 0, 1$. The first object was a thin black cardboard of section 1.8 mm × 8 mm and thickness $s \simeq 400$ μm. A turbid solution with $l^* = 17.3$ mm was used. Figure 3 reports three examples of images recovered via DGI (column 1), diffusive imaging (column 2), and direct imaging (column 3) together with their horizontal sections averaged over the vertical size of the image (column 4). The DGI images were obtained by averaging 10^5 different speckle configurations. The figure shows that, as h increases (top to bottom), the visibility decreases and the measured transmittance in the absorbing $[T(\mathbf{x}) = 0]$ part of the object passes from $T_m \simeq 0.16$ ($h = 3.3$ mm) to $T_m \simeq 0.46$ ($h = 11.3$ mm). While the matching between DGI and diffusive imaging is excellent (although DGI is somewhat noisier, as expected [7]), the

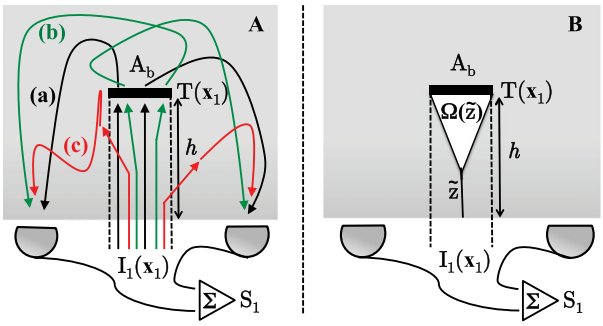

FIG. 4 (color online). (Panel A) Backscattering scheme showing that the bucket signal S_1 is composed by three main contributions: (a) straight light hitting the object at a depth h, (b) forward scattered light that illuminates the object, and (c) scattered light collected without intercepting the object. (Panel B) Scheme for the fraction ε_h of the light scattered in the forward direction that hits the object.

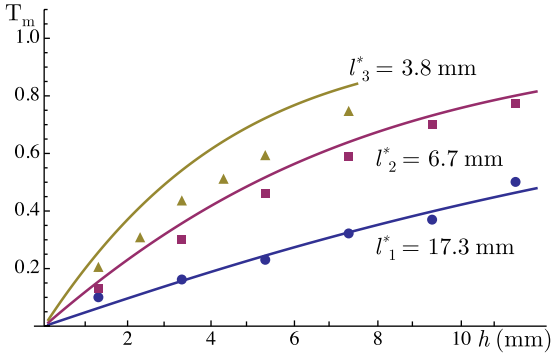

FIG. 5 (color online). Plots of the experimental data (symbols, dimensions equivalent to error bars) and theory (solid curves) for T_m in the zones where $T(\mathbf{x}) = 0$ as a function of the depth h, for three different turbid solutions.

contrast of the images retrieved with direct imaging is definitely much smaller. This occurs since direct illumination produces retrodiffused light originating at the object interface, which creates a spurious offset in the measured transmission. The blue dashed lines in column 4 derive from a simple model for DGI described below.

Under the assumption of a thin object of thickness s, located at a depth h from the entrance face of the cell such that $s \ll h \ll l^*$, the light travelling along the distance h can be considered as undergoing only single scattering events. Thus, the light that hits the object (as sketched in panel A of Fig. 4) is made of two main contributions: (2a) the straight nonscattered light that reaches the object with a probability $\beta_h = \exp(-h/l^*)$ given by the Lambert-Beer (LB) law [16], and (2b) the light that, after being scattered with probability $1 - \beta_h$, reaches the object with a probability ε_h determined by geometrical factors. Hence, we may write this intensity as

$$I_1^{(h)}(\mathbf{x_1}) = \beta_h I_1(\mathbf{x_1}) \tag{2a}$$

$$+ (1 - \beta_h)\varepsilon_h \frac{\int_{A_b} I_1(\mathbf{x}_1')d\mathbf{x}_1'}{A_b} i_{sc}(\mathbf{x_1}), \tag{2b}$$

where $\int_{A_b} I_1(\mathbf{x}_1')d\mathbf{x}_1'/A_b$ is the incident average intensity and $i_{sc}(\mathbf{x_1})$ is the distribution of the scattered light, totally uncorrelated to $I_1(\mathbf{x_1})$, normalized so that $\int_{A_b}\langle i_{sc}(\mathbf{x_1})\rangle d\mathbf{x_1}/A_b = 1$. The bucket signal S_1 is given by $\int_{A_b} I_1^{(h)}(\mathbf{x_1})T(\mathbf{x_1})d\mathbf{x_1}$ plus a third term coming from the scattered light that does not pass through the object:

$$S_1 \propto \Big\{\beta_h \int_{A_b} T(\mathbf{x_1})I_1(\mathbf{x_1})d\mathbf{x_1} \tag{3a}$$

$$+ (1 - \beta_h)\varepsilon_h \frac{\int_{A_b} I_1(\mathbf{x}_1')d\mathbf{x}_1'}{A_b} \int_{A_b} i_{sc}(\mathbf{x_1})T(\mathbf{x_1})d\mathbf{x_1} \tag{3b}$$

$$+ (1 - \beta_h)(1 - \varepsilon_h) \int_{A_b} I_1(\mathbf{x_1})d\mathbf{x_1}\Big\}. \tag{3c}$$

Note that if the object is placed on the surface ($h = 0$), $\beta_0 = 1$, we recover the common definition of the bucket signal (3a) used in the absence of the turbid medium, regardless of ε_h. The dimensionless factor $\varepsilon_h = \frac{1}{h}\int_0^h d\tilde{z}\beta_{\tilde{z}}\omega(\tilde{z}, h)$ is an average along the object depth h of the probability $\omega(\tilde{z}, h)$ that light scattered at a distance $\tilde{z}$ from the cell surface hits the object, weighted by the LB factor $\beta_{\tilde{z}}$ (see panel B of Fig. 4). This probability corresponds to the fraction of light scattered within a maximum solid angle $\Omega(\tilde{z})$ subtended by the object and is given by $\omega(\tilde{z}, h) = \frac{3}{8\pi}\int_{\Omega(\tilde{z})} \sin^2\phi d\Omega$. We assume Rayleigh scattering with an incident polarized electric field that forms an angle ϕ with the scattering direction. The factor ε_h is computed numerically.

Combining Eqs. (1) and (3), with the assumption of uniform illumination $[\langle I_1(\mathbf{x_1})\rangle = \langle I_1\rangle,\ \langle I_2(\mathbf{x_2})\rangle = \langle I_2\rangle]$, and taking into account that $I_2(\mathbf{x_2})$ and $i_{sc}(\mathbf{x_1})$ are uncorrelated $[\langle I_2(\mathbf{x_2})i_{sc}(\mathbf{x_1})\rangle = \langle I_2(\mathbf{x_2})\rangle\langle i_{sc}(\mathbf{x_1})\rangle = \langle I_2\rangle]$, we derive an expression for the measured transmittance of the object $T_m(\mathbf{x})$ in terms of the true $T(\mathbf{x})$:

$$T_m(\mathbf{x}) = \beta_h T(\mathbf{x}) + (1 - \beta_h)[\varepsilon_h \overline{T} + 1 - \varepsilon_h], \tag{4}$$

where $\overline{T} = \int_{A_b} T(\mathbf{x_1})d\mathbf{x_1}/A_b$ is the spatially averaged transmittance of the object. As expected, Eq. (4) predicts that, in the case of nonturbid media or in the case of objects placed at the surface of the cell, whenever $h/l^* \to 0$, $T_m(\mathbf{x}) \to T(\mathbf{x})$. But remarkably, although based on the assumption that $h \ll l^*$, Eq. (4) predicts also the correct behavior of $T_m(\mathbf{x})$ for highly turbid media or objects deeply inside the scattering cell ($h/l^* \to \infty$), for which $\beta_h \to 0$ and $\varepsilon_h \to 0$. In these cases, indeed, the object becomes invisible and, consistently, Eq. (4) predicts $T_m(\mathbf{x}) \to 1$. When Eq. (4) is applied to the analysis of the images of Fig. 3 (blue dashed lines in column 4), the agreement with the experimental data is excellent in the zones where $T(\mathbf{x}) = 0$, while is somewhat less accurate where $T(\mathbf{x}) = 1$. Overall, the simple model of Eqs. (2) and (3) is able to capture the essential physics of DGI in turbid

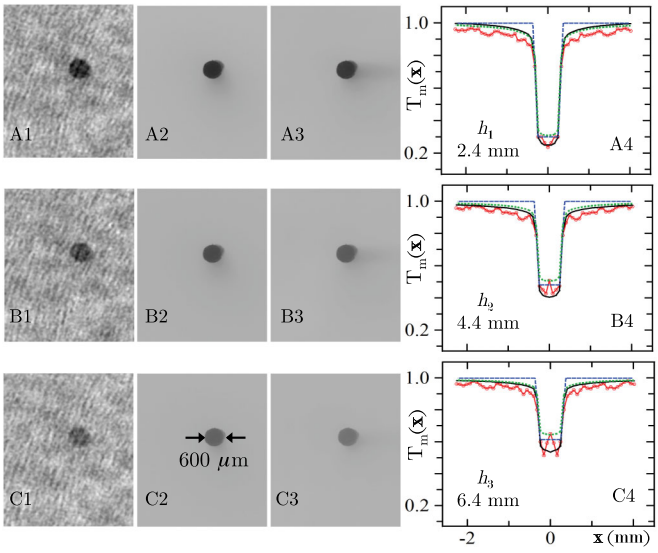

FIG. 6 (color online). Images of a small absorbing sphere (diameter = 600 μm) inside a turbid solution with $l^* = 6.7$ mm at $h_1 = 2.4$ mm (row A), $h_2 = 4.4$ mm (row B), and $h_3 = 6.4$ mm (row C), obtained with DGI (column 1), diffusive imaging (column 2), and direct imaging (column 3). Column 4 plots the radial profiles averaged over the azimuthal angles: DGI (red wavy curve), direct imaging (green dotted curve), diffusive imaging (black smooth curve), and theoretical model (blue dashed line).

media. In Fig. 5 we compare the experimental data with the theoretical predictions [Eq. (4)] for T_m in the absorbing part of the object, as a function of h for three different turbidities. The agreement, quite good at low turbidity ($l^* = 17.3$ mm), becomes less accurate at higher turbidity ($l^* = 3.8$ mm), where multiple scattering reduces the validity of the model assumptions.

Our results were also validated by measuring an absorbing sphere much smaller (diameter = 600 μm) than the beam area (so that $\overline{T} \simeq 0.99$) in a turbid solution with $l^* = 6.7$ mm. Figure 6 reports the images retrieved with DGI (column 1), diffusive imaging (column 2), and direct imaging (column 3), together with their corresponding radial profiles (column 4) obtained by averaging the images over the azimuthal angles. As for Fig. 3, the object becomes less visible as h is increased. In the zones where $T(\mathbf{x}) = 0$ we obtain values that range from $T_m \simeq 0.30$ ($h_1 = 2.4$ mm) to $T_m \simeq 0.61$ ($h_3 = 6.4$ mm), a result that is equivalent for both DGI and diffusive imaging. Again, the two techniques are more accurate than direct imaging, even though the effect is less evident because $\overline{T} \sim 1$. The agreement between the experimental results and the theoretical model is excellent, as shown in column 4 of the figure.

In this Letter we have shown that DGI can be profitably used in a backscattering configuration for the imaging of small absorbing objects immersed in a turbid medium, in proximity of its surface. DGI recovers images with much better contrast than noncorrelated direct imaging, which is the technique commonly used in biomedical imaging of superficial tissues. In the attempt to assess its performances, we have also compared DGI with an innovative imaging method that we called *diffusive imaging*, where the object, similarly to what done in Ref. [14], is transilluminated by the light diffused by the turbid medium. Our results show that DGI and diffusive imaging perform almost identically, i.e., they provide the correct transmission function when the object is located on the surface, and are equally affected by the increasing presence of scattering as the object is moved deeper inside the medium. Thus, DGI and diffusive imaging represent two simple optical methods capable of sensing directly object absorption, a feature that can be found only in rather complex techniques such as time-gating detection [17], tomographic techniques (diffusive optical tomography [18], laminar optical tomography [19], optical projection tomography [20]), or photoacoustic microscopy [21]. We therefore believe that backscattering DGI has the potentialities to become, in the near future, a simple valid imaging tool that is an alternative or complement to the current state-of-the-art biofunctional imaging techniques. Finally, but not less important, our results provide a clear contribution to the current debate about the presumed *immunity* of GI to scattering or turbulence. They show that indeed DGI is not immune from scattering, exactly as in the case of GI when there is turbulence between the beam splitter and the object or the CCD [11].

The authors acknowledge T. Durduran, A. Pifferi, F. Scheffold, and R. Cerbino for helpful discussions, and M. Pigazzini for the loan of the macro objective. M. B. acknowledges funding from Regione Lombardia (UNIRE Program, DRR n.85/2011) and support from Quanta System S.p.a.

*matteo.bina@gmail.com
†Present address: Light in Light s.r.l. via Ferrari 14, I-22100 Como, Italy.

[1] T. B. Pittman, Y. H. Shih, D. V. Strekalov, and A. V. Sergienko, Phys. Rev. A **52**, R3429 (1995).
[2] J. H. Shapiro and R. W. Boyd, Quantum Inf. Process. **11**, 949 (2012), and references therein.
[3] F. Ferri, D. Magatti, A. Gatti, M. Bache, E. Brambilla, and L. A. Lugiato, Phys. Rev. Lett. **94**, 183602 (2005).
[4] B. I. Erkmen and J. H. Shapiro, Phys. Rev. A **77**, 043809 (2008).
[5] J. H. Shapiro, Phys. Rev. A **78**, 061802(R) (2008).
[6] O. Katz, Y. Bromberg, and Y. Silberberg, Appl. Phys. Lett. **95**, 131110 (2009).
[7] F. Ferri, D. Magatti, L. A. Lugiato, and A. Gatti, Phys. Rev. Lett. **104**, 253603 (2010).
[8] N. D. Hardy and J. H. Shapiro, Phys. Rev. A **84**, 063824 (2011); P. B. Dixon *et al.*, Phys. Rev. A **83**, 051803(R) (2011).
[9] N. Tian, Q. Guo, A. Wang, D. Xu, and L. Fu, Opt. Lett. **36**, 3302 (2011).

[10] W. Gong and S. Han, Opt. Lett. **36**, 394 (2011).
[11] R. E. Meyers, K. S. Deacon, and Y. Shih, Appl. Phys. Lett. **98**, 111115 (2011); J. Shapiro, arXiv:1201.4513v1.
[12] R. Cerbino, Phys. Rev. A **75**, 053815 (2007); A. Gatti, D. Magatti, and F. Ferri, Phys. Rev. A **78**, 063806 (2008); D. Magatti, A. Gatti, and F. Ferri, Phys. Rev. A **79**, 053831 (2009).
[13] F. Ferri, D. Magatti, V. G. Sala, and A. Gatti, Appl. Phys. Lett. **92**, 261109 (2008).
[14] T. N. Ford, K. K. Chu, and J. Mertz, Nat. Methods **9**, 1195 (2012).
[15] G. Fabbrocini *et al.*, Open Dermatol. J. **4**, 110 (2010).
[16] H. C. Van de Hulst, *Light Scattering by Small Particles* (Dover Publications, New York, 1957).
[17] C. Dunsby and P. M. W. French, J. Phys. D **36**, R207 (2003).
[18] T. Durduran, R. Choe, W. B. Baker, and A. G. Yodh, Rep. Prog. Phys. **73**, 076701 (2010).
[19] E. M. C. Hillman, D. A. Boas, A. M. Dale, and A. K. Dunn, Opt. Lett. **29**, 1650 (2004).
[20] J. Sharpe, U. Ahlgren, P. Perry, B. Hill, A. Ross, J. Hecksher-Sørensen, R. Baldock, and D. Davidson, Science **296**, 541 (2002).
[21] H. F. Zhang, K. Maslov, G. Stoica, and L. V. Wang, Nat. Biotechnol. **24**, 848 (2006).